INORGANIC CHEMISTRY FRONTIERS

CCS 中国化学会 CHINESE CHEMICAL SOCIETY

ROYAL SOCIETY OF CHEMISTRY

Electrocatalytic Hydrogen Evolution and Doping Modification of Weyl Semimetal PtBi2 Acidic Solution

Journal:	*Inorganic Chemistry Frontiers*
Manuscript ID	QI-RES-01-2025-000022.R1
Article Type:	Research Article
Date Submitted by the Author:	18-Feb-2025
Complete List of Authors:	Liu, Yinghui; Tianjin University of Technology Chen, Qiubo; Institute of High Performance Computing, Materials Science & Chemistry An, Yukai; Tianjin University of Technology Qiu, Hailong; Tianjin University of Technology, Tianjin Key Laboratory of Functional Crystal Materials, Institute of Functional Crystal Ma, Shihui; Tianjin University of Technology Liu, Hongjun; Tianjin University of Technology Hu, Zhanggui; Tianjin University of Technology, Tianjin University of Technology Wu, Yicheng; Tianjin University of Technology, Functional Crystal Materials

ARTICLE

Electrocatalytic Hydrogen Evolution and Doping Modification of Weyl Semimetal $PtBi_2$ Acidic Solution

Received 00th January 20xx,
Accepted 00th January 20xx

DOI: 10.1039/x0xx00000x

Yinghui Liu[a], Chen Qiubo[b], Yukai An[c], Hailong Qiu*[a], Shihui Ma*[a], Hongjun Liu[a], Zhanggui Hu[a] and Yicheng Wu[a]

We synthesized centimeter-scale type-Ⅰ Weyl semimetal layered trigonal $PtBi_2$ (t-$PtBi_2$) crystals, including intrinsic and doped with diverse elements. Electrocatalytic hydrogen evolution tests were conducted in acidic solutions, allowing for a comparative analysis of their performance against commercial Pt/C electrodes. The results demonstrated that the hydrogen evolution activity of the synthesized topological semimetal crystals significantly surpassed that of the commercial Pt/C electrodes. Furthermore, the introduction of various dopants further enhanced the hydrogen evolution performance of the crystals. Besides, the first principle calculations confirmed these findings and were consistent with the experimental data. This research contributes valuable insights into the potential applications of topological semimetals in electrocatalytic hydrogen evolution.

Introduction

As the global energy demand continues to rise, humanity faces the pressing challenge of transitioning from non-renewable fossil fuels, such as oil and gas, to renewable and environmentally friendly energy sources.[1-3] Among various alternatives, the process of generating hydrogen gas through electrocatalytic water splitting has emerged as a promising area of research with significant potential for practical applications.[4-6] In recent years, topological materials have become a focal point in electrocatalysts, garnering attention for their remarkable properties, including extensive topological surface states and high carrier mobility.[7-11] These unique characteristics make them particularly suited for enhancing the efficiency of electrocatalytic processes.[7, 12-17] Researchers are actively exploring using semimetals as catalysts in this context.[18-22] A noteworthy study conducted in 2004 calculated the potential of over 100 binary compounds as electrocatalysts through first-principles calculations.[23] The findings highlighted the exceptional performance of intermetallic ordered compounds like platinum-bismuth (PtBi) as promising catalyst electrode materials. Building on this foundation, researchers have successfully synthesized nanoscale crystals such as PtBi[24] and $PtBi_2$ [25, 26], demonstrating impressive efficacy in methanol electrooxidation and carbon dioxide separation processes.[25] Previous investigations have established that the Weyl semimetal material $PtBi_2$ exhibits outstanding characteristics in electrochemical catalysis. The study by Kuibarov et al. presents angle-resolved photoemission spectroscopy (ARPES) characterization data for $PtBi_2$, demonstrating the existence of topological surface states within this material. This finding contributes to understanding the electronic properties and potential applications of $PtBi_2$ in topological material research. [27] However, a significant knowledge gap remains regarding the application of larger, centimeter-sized crystals in hydrogen evolution reactions during water electrolysis. This presents an exciting opportunity for further exploration and innovation in the field, as combining these larger crystalline structures with effective catalysis could pave the way for more efficient hydrogen production technologies. Furthermore, we have referenced several recent studies that explore the intricate interplay between defects, edge states, and catalytic activity in topological materials such as Weyl semimetals.[28, 29] By systematically investigating these phenomena, our work contributes to a more comprehensive understanding of optimizing the electronic characteristics of $PtBi_2$, thereby paving the way for its application in efficient energy conversion technologies. Through these insights, we aspire to furnish a robust framework for future research to enhance HER catalysts and broaden the practical applications of materials characterized by Weyl semimetal properties.

In this article, we report the successful growth of high-quality t-$PtBi_2$ single crystals via the self-flux method. These crystals belong to the P31m space group and exhibit a layered triangular structure.[30, 31] The resulting crystals are classified under the P31m space group and possess a distinctive layered triangular structure that is noteworthy in their design. To verify the quality of the synthesized crystals, we employed advanced characterization techniques, including X-ray diffraction (XRD) and high-resolution transmission electron

[a.] *Tianjin Key Laboratory of Functional Crystal Materials, Institute of Functional Crystal, Tianjin University of Technology, Tianjin 300384, China.*
E-mail: qiu@tjut.edu.cn, shihuima@email.tjut.edu.cn.
[b.] Institute of High Performance Computing, Agency for Science, Technology and Research, Singa-pore 138632, Republic of Singapore.
[c.] School of Materials Science and Engineering, Tianjin University of Technology, Tianjin 300384, China.
Supplementary Information available: [details of any supplementary information available should be included here]. See DOI: 10.1039/x0xx00000x

microscopy (HRTEM). These methods confirmed that the t-$PtBi_2$ single crystals met high standards of purity and structural integrity. We proceeded to evaluate the electrocatalytic properties of these crystals specifically for hydrogen evolution reactions in 0.5 M H_2SO_4 acidic solutions.[32] In comparative tests against the established commercial catalyst Pt/C, our findings showed that the t-$PtBi_2$ single crystal exhibited impressive electrocatalytic performance, surpassing expectations for hydrogen evolution efficiency. Furthermore, we explored the manipulation of stoichiometric ratios in our crystal synthesis by incorporating different amounts of palladium (Pd), nickel (Ni), and lead (Pb) into the matrix of the t-$PtBi_2$. This doping process, conducted through the self-flux method, was also followed by rigorous characterization via XRD and HRTEM, which confirmed that these modified crystals retained their high quality. The comparative analysis of the hydrogen evolution test data indicated that the performance of the crystals was significantly improved with doping, highlighting the potential of these materials in enhancing electrocatalytic activity. Moreover, the *d*-band center position can be a descriptor for adsorption strength on catalytic surfaces.[33] As the d-band center shifts downward, the binding strength typically weakens. Our calculations show that the *d*-band center of Pt is -2.66 eV, while for $PtBi_2$ is -3.01 eV. This downward shift in the *d*-band center suggests that $PtBi_2$ could exhibit promising catalytic performance. To address this, we conducted additional DFT calculations comparing bulk Pt and $PtBi_2$. our calculations determined hydrogen binding energies of -0.26 eV and 0.08 eV for Pt(111) and $PtBi_2$(001) surfaces, shown in Figure S26. For optimal HER performance, the hydrogen binding energy should approach zero. Therefore, the superior performance of $PtBi_2$ can be attributed to its more favorable electronic structure in the bulk state. Overall, our research provides valuable insights into the synthesis and application of t-$PtBi_2$ single crystals in energy-related catalysis.

Results and discussion

We successfully synthesized high-quality layered trigonal $PtBi_2$ single crystals, exhibiting a configuration analogous to that described in the relevant literature, and subsequently doped the grown crystals, as presented in Fig. S1. The crystallographic configuration is illustrated in Fig. 1(a). Initial observations using scanning electron microscopy (SEM) indicated that the surface of the crystals is relatively flat. The doping ratios of Ni and Pd within the grown crystals were determined through energy-dispersive X-ray spectroscopy (EDS), as demonstrated in Table S1(Ni) and Table S2(Pd). However, the precise quantification of these elements was challenging due to the spectral interference between adjacent lead Pb and Bi elements in the EDS analysis. The element contents of Pb-doped crystals were measured using inductively coupled plasma mass spectrometry (ICP-MS) in Table S3. The diffraction characteristics of the single crystals were analyzed via XRD. As depicted in Fig. 1(b) and Fig. S12-S14, the diffraction peaks corresponding to the (00L) crystal planes of the grown crystals are observable.[31] The (001) crystal plane diffraction peak of $PtBi_2$ is located at an angle of 14.27°, while that of 0.88 at% Pb-$PtBi_2$ appears at 14.3°. The (001) diffraction peak for 1.19 at% Ni-$PtBi_2$ is recorded at 14.39°, and the peak for 1.04 at% Pd-$PtBi_2$ occurs at 14.35° (Fig. 1(c)). The observed shifts in the diffraction peaks are consistent with theoretical predictions regarding the growth behavior of crystals containing dopant elements.

We performed a detailed characterization of the valence states of key elements within the crystal structure utilizing X-ray Photoelectron Spectroscopy (XPS). The results reveal that platinum (Pt) predominantly exists in a zero valence state, alongside a substantial presence of +2 oxidation states[34, 35] shown in Fig. 1(e) and Fig.S15(b)(Pb), S16(b)(Ni), S17(b)(Pd). The binding energy associated with the Pt^0 valence of the $4f_{7/2}$ orbital in $PtBi_2$ is measured at 71.2 eV, while the binding energy for the Pt^{2+} valence is found at 71.78 eV. Furthermore, the binding energy of the Pt^0 valence in the $4f_{5/2}$ orbital registers at 74.53 eV, with the corresponding Pt^{2+} valence at 75.11 eV. In compositions with 0.88 at% Pb-$PtBi_2$, a uniform shift to higher binding energies of 0.09 eV is observed for the $4f_{7/2}$ and $4f_{5/2}$ orbitals pertaining to the Pt^0 and Pt^{2+} valences. For the sample containing 1.19 at% Ni-$PtBi_2$, the same orbitals shift to higher binding energies of 0.25 eV. Similarly, in the 1.04 at% Pd-$PtBi_2$ sample, a shift of 0.13 eV is recorded. These binding energy measurements signal that variations in doping concentrations of distinct elements elicit differential increases in the binding energy of Pt. It is noteworthy that the shifts in the valence states of Pt across different orbitals within the same sample remain consistent, highlighting the interrelated nature of these phenomena.

Bismuth (Bi) predominantly exhibits a valence of 0, with the ability to transition to a +3 oxidation state, while an intermediate +2 oxidation state is also observed[24, 36, 37] as shown in Fig. 1(d) and Fig. S15(a)(Pb), S16(a)(Ni), S17(a)(Pd). The binding energies associated with the Bi^0 valence state of the $4f_{7/2}$ orbital in $PtBi_2$ are measured at 156.9 eV, with the corresponding energies for the Bi^{2+} and Bi^{3+} valence states being 158.36 eV and 158.75 eV, respectively. For the $4f_{5/2}$ orbital, the binding energies for Bi^0, Bi^{2+}, and Bi^{3+} valences are recorded at 162.21 eV, 163.67 eV, and 164.06 eV, respectively. Analysis of the binding energy shifts indicates that for a doping concentration of 0.88 at% Pb-$PtBi_2$, the binding energies for the Bi^0, Bi^{2+}, and Bi^{3+} valence states of the $4f_{7/2}$ and $4f_{5/2}$ orbitals decrease by 0.08 eV, 0.14 eV, and 0.18 eV, respectively. In the case of 1.19 at% Ni-$PtBi_2$, the shifts correspond to 0.27 eV, 0.40 eV, and 0.42 eV, respectively, for the same valence states. Additionally, 1.04 at% Pd-$PtBi_2$ shows binding energy shifts of 0.11 eV, 0.11 eV, and 0.20 eV for the respective states. These findings reveal that variations in the doping concentrations of differing elements markedly influence the binding energy of bismuth, albeit to varying extents. It is noteworthy that the shifts observed in the binding energies of the various valence states of bismuth across different orbitals within the same sample are not uniform. This disparity is likely attributable to the high reactivity of bismuth with atmospheric oxygen.

The binding energies associated with the doped elements in the crystals synthesized with varying elemental compositions are illustrated in Figure 1(f). The observed binding energy spectra for the

different aspects further validate the successful incorporation of dopants during the crystal growth process. Notably, the sample containing Pb in 0.88 at% Pb-$PtBi_2$ exhibited 0 and +2 valence states in the $4f_{7/2}$ and $4f_{5/2}$ orbitals, respectively. Similarly, the measurements of the case of Ni in 1.19 at% Ni-$PtBi_2$ revealed 0 and +2 valence states in the $2p_{3/2}$ orbitals, with +2 valence state detected in the $2p_{1/2}$ orbitals. Moreover, the Pd components analysis in 1.04 at% Pd-$PtBi_2$ showed 0 and +2 valence states in the $3d_{5/2}$ and $3d_{3/2}$ orbitals.[38] Furthermore, the concurrent detection of the $4d_{3/2}$ orbital of Pt can be attributed to its interaction within the specified collection signal range. It is evident from the figure that the binding energy signals corresponding to the three doped elements are relatively weak, a phenomenon that can be attributed to their low concentrations within the samples, as shown in Fig. S15(c)(Pb), S16(c)(Ni), S17(c)(Pd).

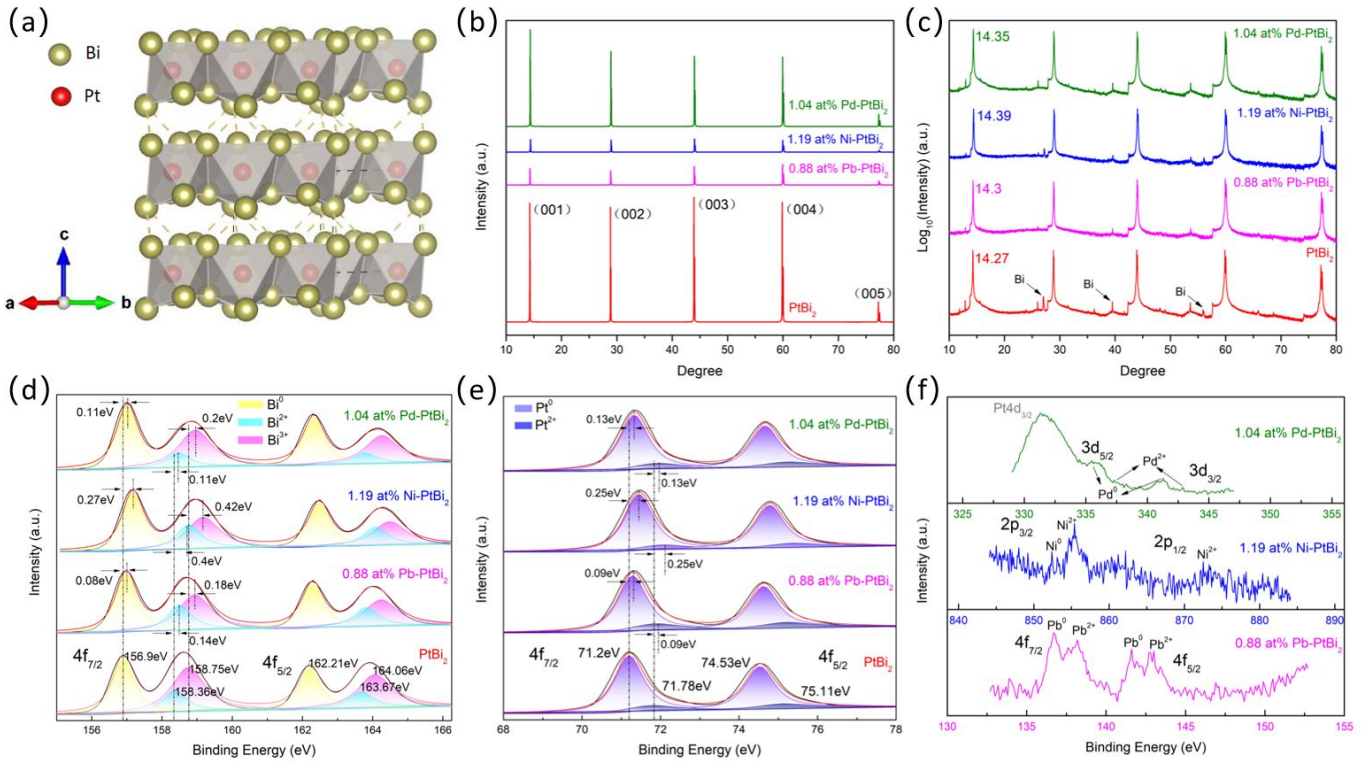

Figure 1. Crystal structure and characterization data. (a) Schematic diagram of the crystal structure of P31m space group γ-$PtBi_2$. (b) Crystal XRD diffraction peak pattern. (c) The logarithmic plot of the XRD diffraction peak intensity of the crystal. (d) XPS characterization of Bi binding energy data for crystals. (e) XPS characte - rization of Pt binding energy data for crystals. (f) XPS characterization of doped element binding energy data in crystals.

To comprehensively assess the growth quality and high-resolution morphology of the crystal, we initiated the process by mechanically exfoliating the crystal onto a silicon wafer following its detachment. The exfoliated material was subsequently wet-transferred onto a copper mesh. We then performed HRTEM analyses. The EDS spectra indicated a uniform distribution of elemental constituents across the sample. Furthermore, the doping elements exhibited a similar uniformity, corroborating the successful growth of high-quality crystals. Subsequent examination of the electron diffraction patterns revealed distinct and well-defined diffraction spots in all crystal orientations, organized in a regular periodic arrangement. This observation further validates the exceptional quality of our crystal growth. We could ascertain the corresponding interplanar spacing associated with each crystal through the processing of high-resolution imaging. The variations in this interplanar spacing effectively underscore the successful incorporation of the doped elements into the crystal lattice.

HRTEM tests were conducted on the samples synthesized along the [0001] crystal band axis direction. The electron diffraction pattern obtained confirms a dense hexagonal structure. The crystal orientation associated with the observed diffraction spots is depicted in the accompanying Figure 2. Fourier transform and inverse Fourier transform analyses were applied to the high-resolution images of the samples to determine their interplanar spacings. The plane spacings for the intrinsic $PtBi_2$ crystals were consistently determined to be 0.57 nm. For the 0.88 at% Pb-$PtBi_2$ samples, the observed plane spacings were 0.56 nm, 0.58 nm, and 0.57 nm, respectively. Similarly, the 1.19 at% Ni-$PtBi_2$ samples exhibited plane spacings of 0.56 nm, 0.56 nm, and 0.57 nm. The 1.04 at% Pd-$PtBi_2$ samples displayed plane spacings of 0.57 nm, 0.58 nm, and 0.57 nm, respectively. Upon a comprehensive analysis of the data, it is observed that the intrinsic $PtBi_2$ crystals exhibit consistent plane spacings when measured along the [0001] crystallographic axes. This observation aligns with the characteristics inherent to the densely packed hexagonal crystal

structure. Additionally, the doping of crystals with three distinct elements, each contributing varying degrees of alteration to the plane spacings, suggests the presence of defects induced by the dopant species. These defects, in turn, result in minor plane spacing perturbations, reflecting the dopants' influence on the crystal lattice.

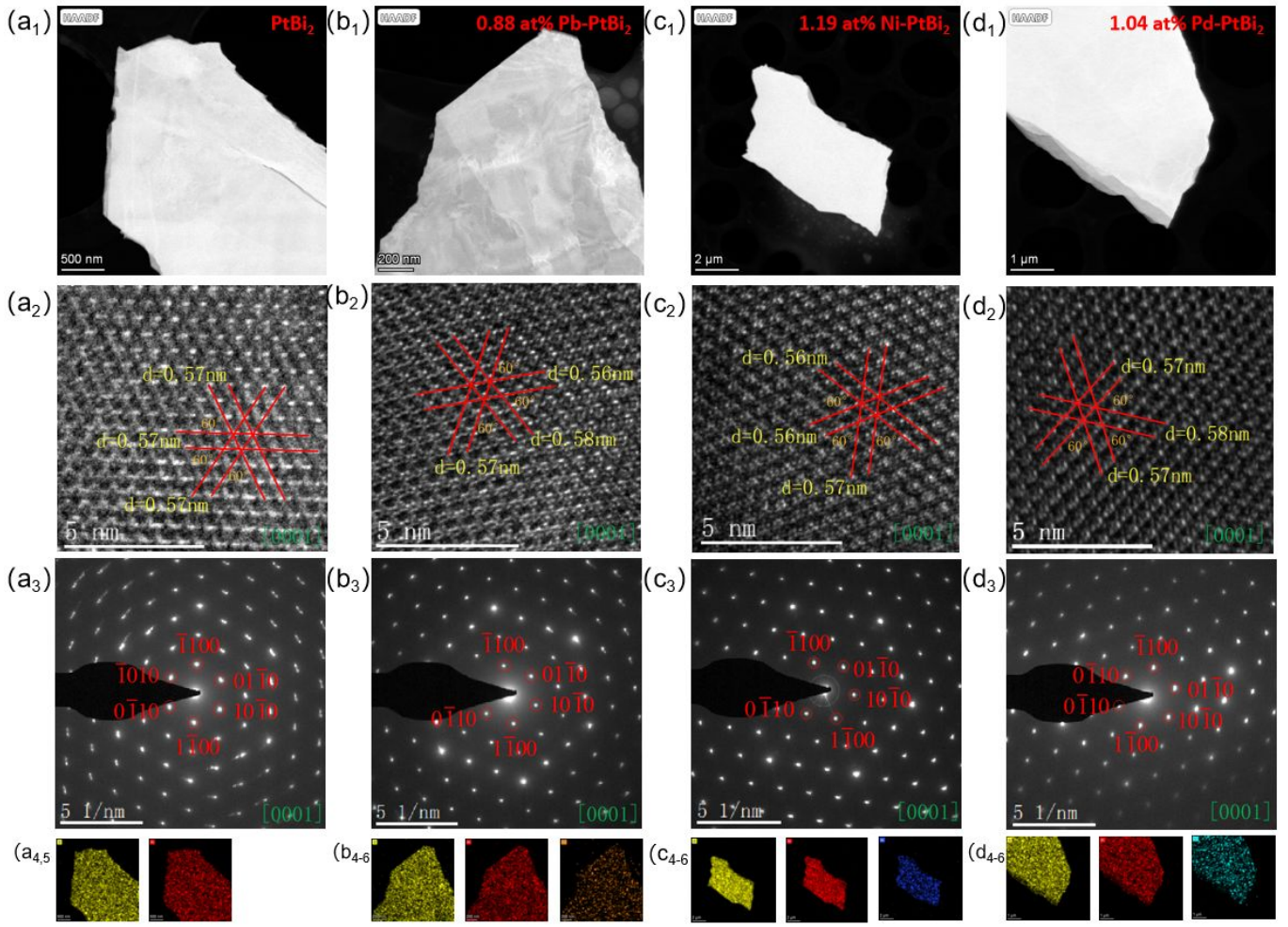

Figure 2. TEM characterization of crystals. ((a-d)$_1$). HAADF-TEM images, ((a-d)$_2$). HRTEM images, ((a-d)$_3$). the SAED patterns, ((a-d)$_{4-6}$). the EDS-mapping images of Bi, Pt, Pb, Ni, and Pd elements of the (a). $PtBi_2$, (b). 0.88 at% Pb-$PtBi_2$, (c). 1.19 at% Ni-$PtBi_2$, and (d). 1.04 at% Pd-$PtBi_2$.

This study presents the results of performance tests on the electrocatalytic hydrogen evolution of synthesized crystals in acidic solutions utilizing a three-electrode system. The catalytic performance of hydrogen precipitation was evaluated across all samples, with the resulting data representing the optimal steady state achieved following the execution of multiple linear sweep voltammetry (LSV) tests. The data signal that the overpotential of $PtBi_2$ at a current density of 10 mA cm^{-2} is 40 mV, which is only marginally 2 mV higher than commercial Pt/C electrodes. Notably, at an overpotential of 96 mV and a current density of 100 mA cm^{-2}, $PtBi_2$ demonstrates a significant reduction in overpotential compared to the 107 mV observed for commercial Pt/C electrodes. The calculated Tafel slope for $PtBi_2$ is 53.6 mV dec^{-1}, marginally lower than the 60.8 mV dec^{-1} for the commercial Pt/C electrode, aligning with the observed overpotential data for both materials. These findings suggest that $PtBi_2$ exhibits superior electrocatalytic activity relative to commercial Pt/C electrodes. Further analysis through cyclic voltammetry (CV) cycling revealed that the double-layer capacitance of $PtBi_2$ is 29.94 mF cm^{-2}, substantially higher than the 4.87 mF cm^{-2} recorded for the commercial Pt/C electrodes. Additionally, electrochemical impedance spectroscopy corroborates that $PtBi_2$ possesses enhanced electrochemical activity compared to its commercial counterparts. In complementary hydrogen evolution catalytic tests, the performance of doped grown crystals was assessed, specifically those with 0.88 at% Pb-$PtBi_2$, 1.19 at% Ni-$PtBi_2$, and 1.04 at% Pd-$PtBi_2$. All variations exhibited improvements that surpassed the performance metrics of commercial Pt/C electrodes. The experimental data underscores that doping during the growth phase can facilitate the generation of additional active sites, thus enhancing the electrocatalytic performance for hydrogen evolution. Finally, a stability test was conducted on the synthesized crystal over a duration of 240 hours, with results indicating that the sample can

maintain consistent and high-performance catalytic activity throughout this extended period. This underscores the potential applicability of $PtBi_2$ in sustainable hydrogen production technologies.

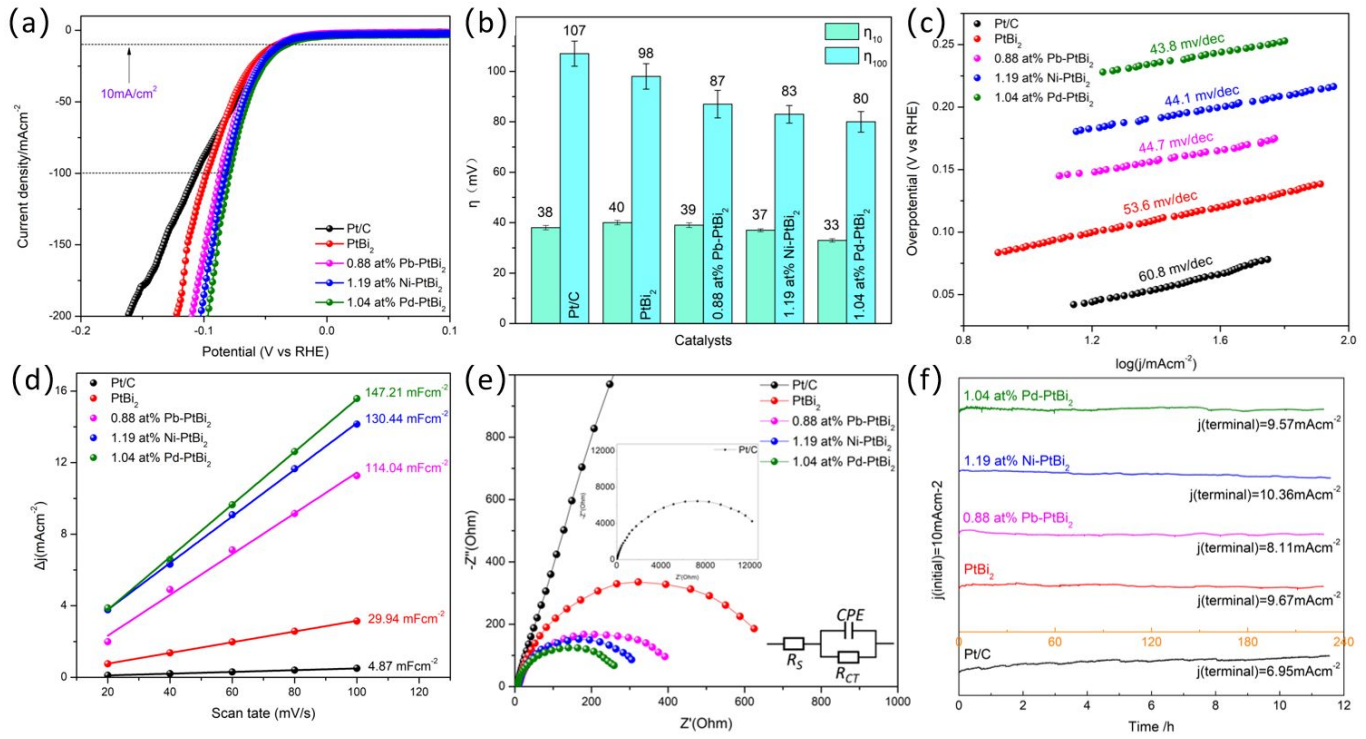

Figure 3. Electrocatalytic performance of the as-prepared commercial Pt/C, $PtBi_2$, 0.88 at% Pb-$PtBi_2$,1.19 at% Ni-$PtBi_2$, and 1.04 at% Pd-$PtBi_2$, for the HER in 0.5 M H_2SO_4. (a) LSV polarization curves. (b) Overpotentials at the 10 and 100 mA cm^{-2} vs. RHE. (c) Tafel plots. (d) The curve of current density with scanning rate. (e) Nyquist plots obtained from electrochemical impedance spectroscopy (EIS) measurements (inset: the integral Nyquist plots of commercial Pt/C and simulated electrochemical equivalent circuit (EEC) for the Nyquist plots). (e) The curve of current density with scanning rate. (f) Long-term stability measurements.

To elucidate the electrocatalytic performance of the synthesized crystals, comprehensive electrochemical measurements were conducted on samples comprising $PtBi_2$, 0.88 at% Pb-$PtBi_2$, 1.19 at% Ni-$PtBi_2$, and 1.04 at% Pd-$PtBi_2$. These experiments utilized a standard three-electrode system in a 0.5 M H_2SO_4 electrolyte and were benchmarked against commercial Pt/C electrodes. All measured potentials were converted from the saturated calomel electrode (SCE) to the reversible hydrogen electrode (RHE) in accordance with the established formula:

$$E_{RHE} = E_{SCE} + 0.2412\text{V} + \text{PH} \times 0.0591.$$

The experimental section provides a thorough outline of the parameters employed throughout the investigations. The findings revealed that the catalytic performance of the synthesized $PtBi_2$ crystals surpassed that of the commercial Pt/C electrodes. Additionally, incorporating dopants—precisely 0.88 at% Pb-$PtBi_2$, 1.19 at% Ni-$PtBi_2$, and 1.04 at% Pd-$PtBi_2$ —further enhanced the electrocatalytic activity. Figure 3(a) illustrates the LSV polarization curves associated with these electrodes. Notably, the overpotential exhibited by $PtBi_2$ at a current density of 10 mA cm^{-2} was measured at 40 mV, representing a marginal increase of only 2 mV compared to the commercial Pt/C electrodes. At a higher current density of 100 mA cm^{-2}, the overpotential of the synthesized crystals was recorded at 96 mV, which demonstrates a significant reduction in comparison to the 107 mV observed for the commercial Pt/C electrodes under identical conditions.

We conducted a systematic investigation into the crystal growth of doped elements, specifically Pb, Ni, and Pd, and evaluated their performance as catalysts for hydrogen evolution reactions. Figure 3(b) illustrates the overpotential associated with these electrodes. The error bars were calculated based on the standard deviation of multiple measurements, ensuring the reliability of our results. The crystal structure doped with lead exhibited superior catalytic performance at a doping concentration of 0.88 at% Pb-$PtBi_2$, demonstrating an overpotential of 39 mV at a current density of 10 mA cm^{-2}. At a higher current density of 100 mA cm^{-2}, the overpotential was recorded at 87 mV. Similarly, the crystal doped with nickel achieved optimal performance at a doping concentration of 1.19 at% Ni-$PtBi_2$, with an overpotential of 37 mV at 10 mA cm^{-2} and an overpotential of 83 mV at 100 mA cm^{-2}. In the case of the palladium-doped crystal, optimal performance was observed at a doping concentration of 1.04 at% Pd-$PtBi_2$, which

yielded an overpotential of 33 mV at 10 mA cm^{-2} and 80 mV at 100 mA cm^{-2}. Comparative analysis of these data indicates that doping can significantly enhance the hydrogen evolution performance of the crystals, achieving lower overpotentials compared to commercial platinum on carbon (Pt/C) electrodes. Notably, the 1.04 at% Pd-$PtBi_2$ sample exhibited the lowest overpotential and the most pronounced improvement relative to commercial alternatives. Additional experimental data pertaining to other doping concentrations are included in the supplementary materials. The test data for crystals with other doping concentrations are included in the Supporting Information Fig.S19(a)(Pb), S21(a)(Ni), S23(a)(Pd).

Evaluating the catalytic kinetics of the hydrogen evolution reaction (HER) through the calculation of the Tafel slope is of paramount importance in elucidating the underlying mechanisms of HER. According to the Tafel equation：

$$\eta = b\log|j| + a.$$

The parameters are defined as follows: *j* denotes the current density, *b* represents the Tafel slope, and *a* signifies the intercept associated with the exchange current density j_0.[39]

The polarization curve corresponding to these measurements was derived via data processing. The Tafel slope for $PtBi_2$ was found to be 53.6 mV dec^{-1}, which is slightly lower than the 60.8 mV dec^{-1} observed for the commercial Pt/C electrode. This observation supports the overpotential data associated with both electrode materials, suggesting a comparative analysis of their electrocatalytic performance. For the doped crystals, the Tafel slopes were measured as follows in the accompanying figure 3(c): 0.88 at% Pb-$PtBi_2$ exhibited a Tafel slope of 44.7 mV dec^{-1}, 1.19 at% Ni-$PtBi_2$ demonstrated a slope of 44.1 mV dec^{-1}, and 1.04 at% Pd-$PtBi_2$ showed a Tafel slope of 43.8 mV dec^{-1}. The observed decrease in Tafel slopes for the doped crystals signals an enhancement in charge transfer kinetics to varying degrees. Notably, the doping concentration exhibiting the minor Tafel slope among the crystals with different dopants is consistent with the overpotential data obtained through LSV.

As the doping concentration of various atoms increases, a corresponding decrease in the Tafel value is observed. At equivalent current densities, a reduced overpotential is required, indicating enhanced charge transfer kinetics. This relationship implies that a lower Tafel slope reflects the catalyst's ability to elicit a rapid electrochemical response at reduced overpotentials. Notably, the Tafel slope associated with the lowest current indicates that the crystals doped with 0.88 at% Pb-$PtBi_2$, 1.19 at% Ni-$PtBi_2$, and 1.04 at% Pd-$PtBi_2$ exhibit superior electrocatalytic kinetics. These catalysts are characterized by low overpotentials and low Tafel slopes, yielding remarkable hydrogen evolution efficiencies. Furthermore, the Tafel slope is valuable for qualitatively assessing the electrocatalytic reaction mechanism. In this context, the HER can be attributed to three potential mechanistic pathways in acidic electrolytes: [40]

$$\text{Volmer step}: \ H^+ + e^- \rightarrow H_{abs}$$

$$b = \frac{2.3RT}{(1+\partial)F} \approx 120 \text{ mV dec}^{-1} \text{ Tafel slope}$$

$$\text{Heyrovsky step}: \ H_{abs} + H^+ + e^- \rightarrow H_2$$

$$b = \frac{2.3RT}{2F} \approx 40 \text{ mV dec}^{-1} \text{ Tafel slope}$$

$$\text{Tafel step}: \ 2H_{abs} \rightarrow H_2$$

$$b = \frac{2.3RT}{\partial F} \approx 30 \text{ mV dec}^{-1} \text{ Tafel slope}$$

In the presented equation, H_{abs} denotes the hydrogen atom that is adsorbed onto the surface of the catalyst. The parameter α, approximately equal to 0.5, functions as the symmetry coefficient. Additionally, *R* represents the ideal gas constant, *F* is the Faraday constant, and T is the absolute temperature.

Hydrogen (H_2) production can occur through two primary mechanisms: the Volmer-Heyrovsky reaction and the Volmer-Tafel reaction. At a controlled temperature of 25°C, the Tafel slopes of 120 mV dec^{-1}, 40 mV dec^{-1}, and 30 mV dec^{-1} are indicative of the respective rate-determining steps in the HER process, corresponding to the Volmer reaction, the Heyrovsky response, and the Tafel reaction. In this investigation, the Tafel slope for the $PtBi_2$ catalyst was determined to be 53.6 mV dec^{-1}, in contrast to the commercial Pt/C electrode, which exhibited a Tafel slope of 60.8 mV dec^{-1}. For Pb-doped crystals, the measured Tafel slope ranged from 44.7 mV dec^{-1} to 55.59 mV dec^{-1}(Fig.3(c) and Fig.S19(b)). Additionally, the Tafel slope for crystals doped with Ni) varied from 44.1 mV dec^{-1} to 70.92 mV dec^{-1}(Fig.3(c) and Fig.S21(b)), while that for Pd doping ranged between 43.8 mV dec^{-1} and 52.5 mV dec^{-1}(Fig.3(c) and Fig.S23(b)). These findings imply that the catalytic pathways delineated in this study predominantly follow the Volmer-Heyrovsky mechanism, with the rate-determining step associated with hydrogen desorption. During the Volmer reaction, protons are rapidly adsorbed from the acidic solution onto the active sites, culminating in the formation of H_{abs}. Subsequently, in the Heyrovsky reaction, solvated protons from the adjacent water layer interact with the surface-adsorbed hydrogen to generate H_2, with the kinetics of surface-bound H_2 formation being the prevailing mechanism.[41, 42] Upon conducting a comparative analysis of the data, it was determined that the Tafel slope of crystals fabricated with doped elements exhibited a reduction to varying extents when contrasted with intrinsic $PtBi_2$. This observation suggests that atomic doping facilitates an increase in active sites on the catalyst surface, optimizes the absorption energy of H^+, and consequently accelerates the performance of the HER. Notably, the Tafel slope for the catalyst with 3.62 at% Ni-$PtBi_2$ is greater than the 53.6 mV

dec^{-1} observed for intrinsic $PtBi_2$, indicating that surpassing the optimal doping concentration may compromise the efficacy of the active sites within the inherent crystal structure. Additionally, the doped crystal with the minimum Tafel slope among the three distinct doped element crystals is characterized by a doping amount that is situated within a mid-range rather than at the maximum level, a phenomenon that consistently persists across the samples evaluated.

The electrochemical active surface area (ECSA) is pivotal in the HER. Typically, the catalytic activity of various catalysts is closely correlated with their ECSA.[43] This article presents an analysis of the electrochemical double-layer capacitance (C_{dl}) at the solid-liquid interface across different scan rates, utilizing CV curves.[44-46] Subsequently, ECSA is derived from the C_{dl} value through the application of the following equation:

$$\mathrm{ECSA} = C_{\mathrm{dl}} / C_s$$

In a 0.5 M H_2SO_4 electrolyte, the commercial Pt/C electrode and various synthesized crystal catalysts were subjected to CV tests at scan rates ranging from 20 to 100 mV s^{-1} as shown in Fig S18. These experiments were performed within a defined potential window for the respective materials. All catalysts exhibited consistent Faradaic behavior and maintained well-defined morphological characteristics. The relationship between scan rate and current density is presented in Figure 3(d). The slope of the fitted line represents the C_{dl} value for each catalyst, serving as a critical parameter for assessing the number of HER active sites available. The data obtained denote that the C_{dl} value for the commercial Pt/C electrode is 4.87 mF cm^{-2}, whereas the C_{dl} value for $PtBi_2$ is significantly elevated at 29.94 mF cm^{-2}. Furthermore, the C_{dl} values for crystals synthesized through doping strategies have shown marked increases. Notably, the 0.88 at% Pb-$PtBi_2$ exhibited the highest enhancement, with a C_{dl} value of 114.04 mF cm^{-2}. The 1.19 at% Ni-$PtBi_2$ demonstrated a C_{dl} value of 130.44 mF cm^{-2}, and the 1.04 at% Pd-$PtBi_2$ with a C_{dl} value of 147.21 mF cm^{-2}. The test data for crystals with other doping concentrations are included in the Supporting Information Fig.S19(c)(Pb), S21(c)(Ni), and S23(c)(Pd). These electrochemical findings substantiate the conclusion that the doped crystalline structures possess a significantly larger electrochemical active surface area for electrocatalysis, indicating an increased density of HER active sites. Consequently, these results imply that the corresponding catalysts demonstrate enhanced catalytic performance.

Figure 3 (e) illustrates the corresponding Nyquist plot alongside its equivalent circuit representation(Illustration: Integral Nyquist plot of commercial Pt/C and simulated electrochemical equivalent circuit (EEC) of Nyquist plot [47]). In this analysis, R_s denotes the uncompensated series resistance, while the constant phase element (*CPE*) represents the double-layer capacitance under HER conditions. R_{ct} signifies the charge transfer resistance associated with the HER process.[48] In the context of the Nyquist plot, the diameter of the semicircle is indicative of the R_{ct}, which reflects the electrocatalytic kinetics occurring at the interface between the electrocatalyst and the electrolyte.[49] A reduced R_{ct} value correlates with an increased charge transfer rate and enhanced conductivity. Observations reveal that the charge transfer resistance of commercial Pt/C electrodes is 10^5 ohms, whereas the charge transfer resistance of the synthesized crystal materials is significantly lower, approximately 10^2 ohms. The test data for crystals with other doping concentrations are included in the Supporting Information Fig.S19(d)(Pb), S21(d)(Ni), and S23(d)(Pd). The findings suggest that the charge transfer resistance intrinsic to our crystal system is significantly lower than that observed in commercial Pt/C electrodes. Additionally, a comparative analysis between the pure $PtBi_2$ crystal and its doped derivatives reveals a consistent decline in charge transfer resistance. Notably, the crystal variant doped with 1.04 at% Pd-$PtBi_2$ exhibits the lowest charge transfer resistance recorded among the samples investigated.

The results imply that the doping of elements significantly affects the electronic structure of intrinsic $PtBi_2$ crystals, facilitates charge transfer, and enhances the electron density at active sites, resulting in improved catalytic performance. From an applied perspective, in addition to exhibiting commendable HER performance, the long-term stability of catalysts is a crucial parameter for industrial applicability.[8, 10] A high current density stability test was conducted to ascertain the robustness of the electrocatalytic material. In this context, controlled potential electrolysis measurements were employed to evaluate the stability of the optimal HER catalyst, as depicted in Figure 3(f). The test results demonstrate that the commercial Pt/C electrode exhibits commendable stability throughout a 12-hour testing period. As this electrochemical catalyst is widely recognized and established, it is reasonable to anticipate that it will sustain its stability for an extended duration. Furthermore, we conducted long-term stability tests on the synthesized crystals, specifically $PtBi_2$, 0.88 at% Pb-$PtBi_2$, 1.19 at% Ni-$PtBi_2$, and 1.04 at% Pd-$PtBi_2$, over a period of 240 hours. The enhanced stability of Ni-$PtBi_2$ can be attributed to the superior affinity of nickel for oxygen, which facilitates the formation of a stable oxide layer. This oxide layer plays a crucial role in mitigating surface corrosion when exposed to acidic media, thereby improving the overall durability of the material. In contrast, Pd-$PtBi_2$ exhibits higher initial activity but gradual degradation due to Pd dissolution under prolonged cathodic polarization. However, Pd doping achieves the lowest overpotential, making it optimal for short-term efficiency. We have revised the conclusion to emphasize that Pd doping maximizes activity while Ni doping enhances durability, highlighting the trade-off between performance metrics.[46]

The results denote that our synthesized crystals successfully maintained their catalytic stability over the long term, thereby highlighting their exceptional performance as electrochemical catalysts.

In this letter, we conduct a comparative analysis of the hydrogen precipitation performance of the synthesized topological semimetallic intrinsic $PtBi_2$ and its dopant-element crystals against previously reported other topological materials (Table S5) and Pt-based electrocatalysts (Table S6) utilized as electrocatalytic hydrogen precipitation electrodes in acidic environments. The findings indicate that our synthesized materials exhibit exceptional hydrogen precipitation efficiency coupled with remarkable long-term operational stability. These results substantiate the significant value and impact of our research in electrocatalysis.

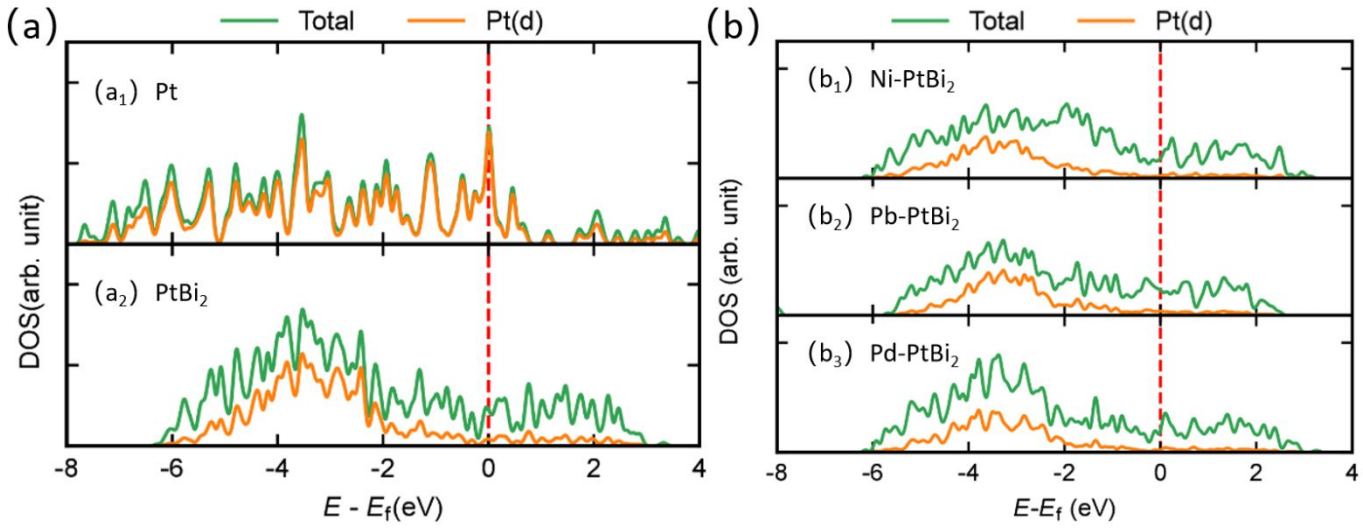

Figure 4. Densify of states of (a) Pt and $PtBi_2$,(b) dopant-$PtBi_2$.

The optimal HER activity is achieved when the Gibbs free hydrogen adsorption energy (ΔG_{H*}) is close to zero. For platinum, the H adsorption on Pt(111) surface is relatively weak, with reported values of -0.27eV[50] and -0.42eV[51]. Modulating the H atom adsorption energy closer to 0.00 eV would lead to optimal catalytic performance. The *d*-band center position can be a descriptor for adsorption strength on catalytic surfaces. As the d-band center shifts downward, the binding strength typically weakens. Our calculations show that the *d*-band center of Pt is -2.66 eV, while $PtBi_2$ is -3.01 eV (Figure 4a). We conducted additional DFT calculations by comparing bulk Pt and $PtBi_2$. The calculations revealed that while the bulk Pt maintains near-neutral charge distribution, the Pt atoms in $PtBi_2$ exhibit more positive charge (0.80|e|), indicating electron transfer from Pt to Bi atoms, shown in Figure S25. This observation aligns with the downward shift of the *d*-band center shown in Figure 4. Furthermore, our calculations determined hydrogen binding energies of -0.26 eV and 0.08 eV for Pt(111) and $PtBi_2$(001) surfaces, shown in Figure S26. For optimal HER performance, the hydrogen binding energy should approach zero. Therefore, the superior performance of $PtBi_2$ can be attributed to its more favorable electronic structure in the bulk state.

We acknowledge the importance of Densify of States (DOS) calculations for doped $PtBi_2$, as shown in Figure 4, with the corresponding *d*-band centers presented in Table S4. The d-band centers of Ni-$PtBi_2$ (-3.04 eV) and Pd-$PtBi_2$ (-3.06 eV) are slightly more negative than that of pristine $PtBi_2$ (-3.01 eV), which aligns with experimental observations. However, for Pb-$PtBi_2$, the calculated d-band center (-2.90 eV) is more positive than $PtBi_2$, suggesting enhanced catalytic activity. This theoretical prediction does not correspond with experimental findings.

Experimental measurements of overpotentials at 10 mA/cm² show similar values across all samples: Pt (38 mV), $PtBi_2$ (40 mV), Pb-$PtBi_2$ (39 mV), Ni-$PtBi_2$ (37 mV), and Pd-$PtBi_2$ (33 mV). The proximity of these values indicates that the d-band centers should be comparable. Additionally, the low doping concentration (below 1 at.%) suggests that the calculated d-band centers may not accurately represent the experimental system due to computational limitations in modeling such dilute dopant concentrations.

Conclusions

In conclusion, we have successfully synthesized centimeter-scale intrinsic t-$PtBi_2$ single crystals and produced high-quality crystals doped with varying Pb, Ni, and Pd concentrations. Notably, when compared with the electrocatalytic hydrogen precipitation characteristics of commercial Pt/C electrodes—exhibiting an overpotential (η_{100}) of 107 mV, Tafel slope of 60.8 mV dec^{-1}, and a C_{dl} of 4.87 mF cm^{-2}—the intrinsic $PtBi_2$ single crystals demonstrated superior performance with an η_{100} of 98 mV, Tafel slope of 53.6 mV dec^{-1}, and an enhanced C_{dl} of 29.94 mF cm^{-2}. Further theoretical insights were garnered through first-principles calculations, which indicated a downward shift in the center position of the *d*-band

center of the $PtBi_2$ crystals, thereby providing a theoretical basis for their commendable catalytic activity in hydrogen precipitation. Among the doped crystals synthesized herein, the 1.04 at% Pd-$PtBi_2$ exhibited the most remarkable hydrogen evolution performance, surpassing the intrinsic $PtBi_2$ crystals across several performance metrics, including an η_{100} of 80 mV, Tafel slope of 43.8 mV de^{-1}, and a significantly increased C_{dl} of 147.21 mF cm^{-2}. This investigation underscores the substantial enhancement in hydrogen evolution activity afforded by doping, particularly highlighting the potential of tailored topological semimetals for advanced electrocatalytic applications. The findings contribute valuable insights into the synthesis of weyl semimetal materials and their practical implementation in electrocatalysis.

Experimental Section

Synthesis of Materials

The sample was prepared in an alumina crucible utilizing the self-flux method, adhering to a stoichiometric ratio of Pt: Bi= 1:4. The crucible was subsequently placed within a quartz tube, which was evacuated to a high vacuum using a molecular pump and subsequently sealed with a hydrogen-oxygen generator. Following this preparation, the test tube was subjected to a controlled thermal treatment within a furnace. The thermal protocol commenced with a temperature ramp of 10 ℃ per minute until 1000 ℃. This temperature was maintained for 24 hours before being cooled to 450 ℃ at a rate of 3 ℃ h^{-1}. Upon achieving 450 ℃, the sample underwent centrifugation to facilitate the separation of the synthesized crystals from excess bismuth. For the growth of doped crystals, various metal elements were incorporated in differing stoichiometric ratios within the initial reagent mixture, while the aforementioned experimental protocol was consistently applied throughout the growth process.

Sample characterization

The phase structure of single crystals synthesized via the self-flux method was systematically analyzed using a high-resolution X-ray diffractometer (Rigaku SmartLab SE), employing Cu Kα radiation (λ = 0.15406 nm). The elemental composition and morphological characteristics of both the pristine and doped $PtBi_2$ single crystals were thoroughly investigated utilizing X-ray photoelectron spectroscopy Thermo Escalab-250Xi), scanning electron microscopy (Hitachi, SU8010), Inductively Coupled Plasma Mass Spectrometry , and optical microscopy (Olympus BX51M). Furthermore, high-resolution imaging and selected area electron diffraction analyses were conducted on the samples using HRTEM.

Electrochemical measurement of hydrogen evolution reaction

Electrochemical measurements are performed utilizing a conventional three-electrode system on an electrochemical workstation, as outlined in (CHI660E). This configuration includes a saturated calomel electrode employed as the reference electrode, a Pt sheet utilized as the auxiliary or counter electrode, and either $PtBi_2$ or doped growth crystals serving as the working electrode. The 0.5 M H_2SO_4 solution is used as the electrolyte, and all measured potentials are converted to the RHE scale. The effective testing area for the $PtBi_2$ or doped growth crystals on self-supporting electrodes is approximately 4-6 mm^2. The HER performance of the material is characterized using LSV at a scanning rate of 5 mV s^{-1}. In addition, electrochemical impedance spectroscopy is conducted across a frequency range of 0.1 Hz to 1 MHz with an applied amplitude of 5 mV. The C_{dl} is estimated within a scanning rate range of 20 to 100 mV s^{-1}. The electrochemical stability of the materials is rigorously evaluated over periods of 12 and 240 hours using current-time (i-t) curves at a current density of 10 mA cm^{-2}. In order to reduce the impact of uncompensated resistance, all measured potentials and voltages are subjected to an 85% IR correction. This comprehensive approach ensures accurate and reliable characterization of the electrochemical properties of the materials under investigation.

DFT calculations

Ab initio DFT calculations were performed by applying the projector augmented-wave method [52] as implemented in the Vienna Ab initio Simulation Package (VASP).[53] The calculations were performed using a plane-wave cutoff energy of 450 eV. For structural optimization and electronic calculations, Monkhorst-Pack k-point grids of 6×6×6 and 4×4×4 were employed for bulk Pt and $PtBi_2$, respectively. All the atoms were allowed to relax. During the relaxation process, the atoms are adjusted until the total energy reaches a tolerance of 1×10^{-5} eV, ensuring that the forces on each atom are kept below 0.02 eV/Å. The hydrogen binding energy calculations were performed using two different surface models. For Pt(111), a 4×4 supercell with four atomic layers was constructed, with the bottom two layers fixed. For $PtBi_2$(001), a 1×1 supercell with four atomic layers was used, with the bottom three layers fixed. A vacuum layer of 15 Å was implemented for both systems, and dipole corrections were applied.[54]

The Hydrogen adsorption free energy Δ*G*(H*) calculation is defined as

$$\Delta G(\mathrm{H}^*) = G(\mathrm{H}^*) - G(*) - 1/2G(\mathrm{H}_2)(1)$$

Where *G*(H*), *G*(*) and *G*(H_2) are the free energy of surface adsorbed with H atom, slab and H_2 molecule, respectively.

The Gibbs free energies (*G*) at 298.15 K and 1 atm are calculated by:

$$G = E + \Delta ZPE - TS(2)$$

Where *E* is the potential energy obtained from DFT calculations, ΔZP*E* and *S* are the contributions to the free energy

from the zero point vibration energy and entropy, respectively. *T* is the temperature (298K). $G(\mathrm{H}^+ + \mathrm{e}^-)$ is considered as the half of free energy $G(H_2)$.

Author contributions

We strongly encourage authors to include author contributions and recommend using CRediT for standardised contribution descriptions. Please refer to our general author guidelines for more information about authorship.

Conflicts of interest

There are no conflicts to declare.

Acknowledgements

This work was supported by the National Key Laboratory of Infrared Detection Technologies (IRDT-24-10) and the Natural Science Foundation of China (51972229).

References

1. M. Cabán-Acevedo, M. L. Stone, J. R. Schmidt, J. G. Thomas, Q. Ding, H.-C. Chang, M.-L. Tsai, J.-H. He and S. Jin,Efficient hydrogen evolution catalysis using ternary pyrite-type cobalt phosphosulphide,*Nature Materials*, 2015, **14**, 1245-1251.
2. J. Dai, Y. Zhu, Y. Chen, X. Wen, M. Long, X. Wu, Z. Hu, D. Guan, X. Wang, C. Zhou, Q. Lin, Y. Sun, S.-C. Weng, H. Wang, W. Zhou and Z. Shao,Hydrogen spillover in complex oxide multifunctional sites improves acidic hydrogen evolution electrocatalysis,*Nature Communications*, 2022, **13**.
3. Y. Li, Z. G. Yu, L. Wang, Y. Weng, C. S. Tang, X. Yin, K. Han, H. Wu, X. Yu, L. M. Wong, D. Wan, X. R. Wang, J. Chai, Y.-W. Zhang, S. Wang, J. Wang, A. T. S. Wee, M. B. H. Breese, S. J. Pennycook, T. Venkatesan, S. Dong, J. M. Xue and J. Chen,Electronic-reconstruction-enhanced hydrogen evolution catalysis in oxide polymorphs,*Nature Communications*, 2019, **10**.
4. X. Zhu, C. Wang, T. Wang, H. Lan, Y. Ding, H. Shi, L. Liu, H. Shi, L. Wang, H. Wang, Y. Ding, Y. Fu, M. Zeng and L. Fu,Dual Self-Built Gating Boosts the Hydrogen Evolution Reaction,*Advanced Materials*, 2022, **34**.
5. J. Li, J. Hu, M. Zhang, W. Gou, S. Zhang, Z. Chen, Y. Qu and Y. Ma,A fundamental viewpoint on the hydrogen spillover phenomenon of electrocatalytic hydrogen evolution,*Nature Communications*, 2021, **12**.
6. Z. Ji, C. Trickett, X. Pei and O. M. Yaghi,Linking Molybdenum–Sulfur Clusters for Electrocatalytic Hydrogen Evolution,*Journal of the American Chemical Society*, 2018, **140**, 13618-13622.
7. G. Li, C. Fu, W. Shi, L. Jiao, J. Wu, Q. Yang, R. Saha, M. E. Kamminga, A. K. Srivastava, E. Liu, A. N. Yazdani, N. Kumar, J. Zhang, G. R. Blake, X. Liu, M. Fahlman, S. Wirth, G. Auffermann, J. Gooth, S. Parkin, V. Madhavan, X. Feng, Y. Sun and C. Felser,Dirac Nodal Arc Semimetal PtSn4: An Ideal Platform for Understanding Surface Properties and Catalysis for Hydrogen Evolution,*Angewandte Chemie International Edition*, 2019, **58**, 13107-13112.
8. Z. Wang, Z. Lin, Y. Wang, S. Shen, Q. Zhang, J. Wang and W. Zhong,Nontrivial Topological Surface States in Ru3Sn7 toward Wide pH-Range Hydrogen Evolution Reaction,*Advanced Materials*, 2023, **35**.
9. J. Li, M. Hong, L. Sun, W. Zhang, H. Shu and H. Chang,Enhanced Electrocatalytic Hydrogen Evolution from Large-Scale, Facile-Prepared, Highly Crystalline WTe2 Nanoribbons with Weyl Semimetallic Phase,*ACS Applied Materials & Interfaces*, 2017, **10**, 458-467.
10. Q. Yang, G. Li, K. Manna, F. Fan, C. Felser and Y. Sun,Topological Engineering of Pt-Group-Metal-Based Chiral Crystals toward High-Efficiency Hydrogen Evolution Catalysts,*Advanced Materials*, 2020, **32**.
11. Z. He, L. Wang, Y. Liu, Z. Li, X. Dai, G. Liu and X. Zhang,Nodal chain semimetal Co2MnGa: A magnetic catalyst with topological significance,*Chemical Engineering Journal*, 2024, **481**.
12. Y. Wang, Y. Shen, X. Xiao, L. Dai, S. Yao and C. An,Topology conversion of 1T MoS2 to S-doped 2H-MoTe2 nanosheets with Te vacancies for enhanced electrocatalytic hydrogen evolution,*Science China Materials*, 2021, **64**, 2202-2211.
13. Q. Qu, B. Liu, W. S. Lau, D. Pan and I. K. Sou,Highly active hydrogen evolution facilitated by topological surface states on a Pd/SnTe heterostructure,*Cell Reports Physical Science*, 2023, **4**.
14. G. Lin, M. Liang, L. Liu, J. Liu, Z. Ao, Z. Shi and X. Ke,P–P Orbital Interaction Enables Single-Crystalline Semimetallic β-MoTe2 Nanosheets as Efficient Electrocatalysts for Lithium–Sulfur Batteries,*ACS Applied Materials & Interfaces*, 2022, **14**, 55616-55626.
15. G. Li, Y. Sun, J. Rao, J. Wu, A. Kumar, Q. N. Xu, C. Fu, E. Liu, G. R. Blake, P. Werner, B. Shao, K. Liu, S. Parkin, X. Liu, M. Fahlman, S. C. Liou, G. Auffermann, J. Zhang, C. Felser and X. Feng,Carbon-Tailored Semimetal MoP as an Efficient Hydrogen Evolution Electrocatalyst in Both Alkaline and Acid Media,*Advanced Energy Materials*, 2018, **8**.
16. G. Zhou, Y. Shan, Y. Hu, X. Xu, L. Long, J. Zhang, J. Dai, J. Guo, J. Shen, S. Li, L. Liu and X. Wu,Half-metallic carbon nitride nanosheets with micro grid mode resonance structure for efficient photocatalytic hydrogen evolution,*Nature Communications*, 2018, **9**.
17. Y. Sun, J. Wang, Q. Liu, M. Xia, Y. Tang, F. Gao, Y. Hou, J. Tse and Y. Zhao,Itinerant ferromagnetic half metallic cobalt–iron couples: promising bifunctional electrocatalysts for ORR and OER,*Journal of Materials Chemistry A*, 2019, **7**, 27175-27185.
18. H. Ma, X. Huang, L. Li, W. Peng, S. Lin, Y. Ding and L. Mai,Boosting the Hydrogen Evolution Reaction

Performance of P-Doped PtTe2 Nanocages via Spontaneous Defects Formation,*Small*, 2023, **19**.
19. G. Li, J. Huang, Q. Yang, L. Zhang, Q. Mu, Y. Sun, S. Parkin, K. Chang and C. Felser,MoS2 on topological insulator Bi2Te3 thin films: Activation of the basal plane for hydrogen reduction,*Journal of Energy Chemistry*, 2021, **62**, 516-522.
20. L. Li, J. Zeng, W. Qin, P. Cui and Z. Zhang,Tuning the hydrogen activation reactivity on topological insulator heterostructures,*Nano Energy*, 2019, **58**, 40-46.
21. X. Wang, L. Wang, C. Xie, Y. Liu, G. Liu, W. Wang, Z. Cheng, G. Zhang and X. Zhang,Double dual-nodal-line semimetals with large surface density of states: Topological quantum catalysts for the hydrogen-evolution reaction,*Physical Review Applied*, 2023, **20**.
22. L. Wang, X. Zhang, W. Meng, Y. Liu, X. Dai and G. Liu,A topological quantum catalyst: the case of two-dimensional traversing nodal line states associated with high catalytic performance for the hydrogen evolution reaction,*Journal of Materials Chemistry A*, 2021, **9**, 22453-22461.
23. J. Greeley, T. F. Jaramillo, J. Bonde, I. Chorkendorff and J. K. Nørskov,Computational high-throughput screening of electrocatalytic materials for hydrogen evolution,*Nature Materials*, 2006, **5**, 909-913.
24. M. Chu, H. Yang, X. Ye, Y. Qiu, M. Cao, J. Chen, X. Yuan and Q. Zhang,Controllable Construction of PtBi Nanostructures for Enhanced Ethanol Oxidation in Acidic Media,*The Journal of Physical Chemistry C*, 2023, **127**, 8062-8070.
25. X. Zhu, X. Yuan, M. Ge and Y. Tang,Unveil the Potential-Dependent Electrochemical Formate Formation on Topological PtBi2 Monolayer,*ACS Applied Energy Materials*, 2023, **6**, 8677-8683.
26. X. Fu, H. Li, A. Xu, F. Xia, L. Zhang, J. Zhang, D. Ma, J. Wu, Q. Yue, X. Yang and Y. Kang,Phase Engineering of Intermetallic PtBi2 Nanoplates for Formic Acid Electrochemical Oxidation,*Nano Letters*, 2023, **23**, 5467-5474.
27. A. Kuibarov, O. Suvorov, R. Vocaturo, A. Fedorov, R. Lou, L. Merkwitz, V. Voroshnin, J. I. Facio, K. Koepernik, A. Yaresko, G. Shipunov, S. Aswartham, J. v. d. Brink, B. Büchner and S. Borisenko,Evidence of superconducting Fermi arcs,*Nature*, 2024, **626**, 294-299.
28. Y. Lin, X. Chen, Y. Tuo, Y. Pan and J. Zhang,In-situ doping-induced lattice strain of NiCoP/S nanocrystals for robust wide pH hydrogen evolution electrocatalysis and supercapacitor,*Journal of Energy Chemistry*, 2022, **70**, 27-35.
29. L. Wang, D. Wang and Y. Li,Single-atom catalysis for carbon neutrality,*Carbon Energy*, 2022, **4**, 1021-1079.
30. A. Veyrat, V. Labracherie, D. L. Bashlakov, F. Caglieris, J. I. Facio, G. Shipunov, T. Charvin, R. Acharya, Y. Naidyuk, R. Giraud, J. van den Brink, B. Büchner, C. Hess, S. Aswartham and J. Dufouleur,Berezinskii–Kosterlitz–Thouless Transition in the Type-I Weyl Semimetal PtBi2,*Nano Letters*, 2023, **23**, 1229-1235.
31. W. Gao, X. Zhu, F. Zheng, M. Wu, J. Zhang, C. Xi, P. Zhang, Y. Zhang, N. Hao, W. Ning and M. Tian,A possible candidate for triply degenerate point fermions in trigonal layered PtBi2,*Nature Communications*, 2018, **9**.
32. Z. W. Chen, J. Li, P. Ou, J. E. Huang, Z. Wen, L. Chen, X. Yao, G. Cai, C. C. Yang, C. V. Singh and Q. Jiang,Unusual Sabatier principle on high entropy alloy catalysts for hydrogen evolution reactions,*Nature Communications*, 2024, **15**.
33. X. Zhang, L. Wang, M. Li, W. Meng, Y. Liu, X. Dai, G. Liu, Y. Gu, J. Liu and L. Kou,Topological surface state: Universal catalytic descriptor in topological catalysis,*Materials Today*, 2023, **67**, 23-32.
34. S. Han, Y. Ma, Q. Yun, A. L. Wang, Q. Zhu, H. Zhang, C. He, J. Xia, X. Meng, L. Gao, W. Cao and Q. Lu,The Synergy of Tensile Strain and Ligand Effect in PtBi Nanorings for Boosting Electrocatalytic Alcohol Oxidation,*Advanced Functional Materials*, 2022, **32**.
35. B.-W. Zhang, Y.-X. Jiang, J. Ren, X.-M. Qu, G.-L. Xu and S.-G. Sun,PtBi intermetallic and PtBi intermetallic with the Bi-rich surface supported on porous graphitic carbon towards HCOOH electro-oxidation,*Electrochimica Acta*, 2015, **162**, 254-262.
36. T. Qin, D. Wang, X. Zhang, Y. Wang, N. E. Drewett, W. Zhang, T. Dong, T. Li, Z. Wang, T. Deng, Z. Pan, N. Yue, R. Yang, K. Huang, S. Feng, R. Huang and W. Zheng,Unlocking the Optimal Aqueous δ-Bi2O3 Anode via Unifying Octahedrally Liberated Bi-Atoms and Spilled Nano-Bi Exsolution,*Energy Storage Materials*, 2021, **36**, 376-386.
37. J. Li, L. Guo, N. Lei, Q. Song and Z. Liang,Metallic Bi Nanocrystal-Modified Defective BiVO4 Photoanodes with Exposed (040) Facets for Photoelectrochemical Water Splitting,*ChemElectroChem*, 2017, **4**, 2852-2861.
38. G. Zheng, C. Tan, Z. Chen, M. Wang, X. Zhu, S. Albarakati, M. Algarni, J. Partridge, L. Farrar, J. Zhou, W. Ning, M. Tian, M. S. Fuhrer and L. Wang,Electrically controlled superconductor-to-failed insulator transition and giant anomalous Hall effect in kagome metal CsV3Sb5 nanoflakes,*Nature Communications*, 2023, **14**, 678.
39. Y. Zheng, Y. Jiao, M. Jaroniec and S. Z. Qiao,Advancing the Electrochemistry of the Hydrogen-Evolution Reaction through Combining Experiment and Theory,*Angewandte Chemie International Edition*, 2014, **54**, 52-65.
40. Y. Li, H. Wang, L. Xie, Y. Liang, G. Hong and H. Dai,MoS2 Nanoparticles Grown on Graphene: An Advanced Catalyst for the Hydrogen Evolution Reaction,*Journal of the American Chemical Society*, 2011, **133**, 7296-7299.
41. G. Shao, X.-X. Xue, B. Wu, Y.-C. Lin, M. Ouzounian, T. S. Hu, Y. Xu, X. Liu, S. Li, K. Suenaga, Y. Feng and S. Liu,Template-Assisted Synthesis of Metallic 1T′-Sn0.3W0.7S2 Nanosheets for Hydrogen Evolution

Reaction,*Advanced Functional Materials*, 2020, **30**, 1906069.

42. P. V. Shinde, P. Mane, D. J. Late, B. Chakraborty and C. S. Rout,Promising 2D/2D MoTe2/Ti3C2Tx Hybrid Materials for Boosted Hydrogen Evolution Reaction,*ACS Applied Energy Materials*, 2021, **4**, 11886-11897.
43. C. Tang, W. Wang, A. Sun, C. Qi, D. Zhang, Z. Wu and D. Wang,Sulfur-Decorated Molybdenum Carbide Catalysts for Enhanced Hydrogen Evolution,*ACS Catalysis*, 2015, **5**, 6956-6963.
44. X.-D. Wang, Y.-F. Xu, H.-S. Rao, W.-J. Xu, H.-Y. Chen, W.-X. Zhang, D.-B. Kuang and C.-Y. Su,Novel porous molybdenum tungsten phosphide hybrid nanosheets on carbon cloth for efficient hydrogen evolution,*Energy & Environmental Science*, 2016, **9**, 1468-1475.
45. J. H. Nam, M. J. Jang, H. Y. Jang, W. Park, X. Wang, S. M. Choi and B. Cho,Room-temperature sputtered electrocatalyst WSe2 nanomaterials for hydrogen evolution reaction,*Journal of Energy Chemistry*, 2020, **47**, 107-111.
46. C. C. L. McCrory, S. Jung, J. C. Peters and T. F. Jaramillo,Benchmarking Heterogeneous Electrocatalysts for the Oxygen Evolution Reaction,*Journal of the American Chemical Society*, 2013, **135**, 16977-16987.
47. T. Yu, Q. Chen, H. Qiu, H. Liu, Z. Hu and Y. Wu,The effect of Sc doping on the electrocatalytic and optoelectronic properties of 2D SiAs single crystals,*Inorganic Chemistry Frontiers*, 2024, **11**, 3334-3347.
48. K. S. Bhat and H. S. Nagaraja,Nickel selenide nanostructures as an electrocatalyst for hydrogen evolution reaction,*International Journal of Hydrogen Energy*, 2018, **43**, 19851-19863.
49. N. U. Day, M. G. Walter and C. C. Wamser,Preparations and Electrochemical Characterizations of Conductive Porphyrin Polymers,*The Journal of Physical Chemistry C*, 2015, **119**, 17378-17388.
50. T. Kosmala, A. Baby, M. Lunardon, D. Perilli, H. Liu, C. Durante, C. Di Valentin, S. Agnoli and G. Granozzi,Operando visualization of the hydrogen evolution reaction with atomic-scale precision at different metal–graphene interfaces,*Nature Catalysis*, 2021, **4**, 850-859.
51. N. Arulmozhi, S. Hanselman, V. Tudor, X. Chen, D. van Velden, G. F. Schneider, F. Calle-Vallejo and M. T. M. Koper,Energetics and Kinetics of Hydrogen Electrosorption on a Graphene-Covered Pt(111) Electrode, *Journal of the American Chemical Society Au*, 2023, **3**, 526-535.
52. P. E. Blöchl,Projector augmented-wave method,*Physical Review B*, 1994, **50**, 17953-17979.
53. G. Kresse and J. Furthmüller,Efficiency of ab-initio total energy calculations for metals and semiconductors using a plane-wave basis set,*Computational Materials Science*, 1996, **6**, 15-50.
54. J. Neugebauer and M. Scheffler,Adsorbate-substrate and adsorbate-adsorbate interactions of Na and K adlayers on Al(111),*Physical Review B*, 1992, **46**, 16067-16080.

Data availability

The data supporting this article have been included as part of the Supplementary Information.